Supporting information

pH-responsive self-assembly of amyloid fibrils for dual hydrolase-oxidase reactions

*Marta Díaz-Caballero[1], Susanna Navarro[1], Miquel Nuez-Martínez[2], Francesca Peccati[3], Luis Rodríguez-Santiago[4], Mariona Sodupe[4,5], Francesc Teixidor[2] and Salvador Ventura[1,5]**

[1]Institut de Biotecnologia i de Biomedicina (IBB) and Departament de Bioquímica i Biologia Molecular; Universitat Autònoma de Barcelona; 08193 Bellaterra (Barcelona), Spain.

[2]Institut de Ciència de Materials de Barcelona (ICMAB-CSIC). Campus UAB, 08193 Bellaterra, Barcelona (Spain).

[3]Center for Cooperative Research in Biosciences (CIC bioGUNE), Basque Research and Technology Alliance (BRTA), Bizkaia Technology Park, Building 801A, 48160 Derio (Spain)

[4]Departament de Química, Universitat Autònoma de Barcelona, 08193 Bellaterra (Spain)

[5]ICREA, Passeig Lluís Companys 23, E-08010 Barcelona (Spain)

*Corresponding author: E-mail: salvador.ventura@uab.es

Computational Methods

Molecular dynamics simulations were performed with the Amber suite, using the ff14SB force field.[1] To generate all possible parallel fibrillar architectures of HY8d and H8Ye, we used an in-house code that computes the Cartesian coordinates of steric zippers of any length applying rigid rotations and translations to the coordinates of an individual strand. The length of each β-sheet was set to 20 strands, so that each fibril model is composed of 40 strands. For HY8d and H8Ye, we ran molecular dynamics simulations on the six non-equivalent parallel fibrillar architectures (**Figure S13**) and computed their relative energies on 100 frames sampled with a constant stride. A slow equilibration protocol was set up to relax the initial fibrillar architecture to a temperature of 300 K. Since the initial inter-sheet distance is set to a large value to avoid steric clashes, equilibration involves short low temperature unrestrained dynamics bursts to allow the fibril model to pack side chains at the steric zipper. The geometry of all fibril models after 100 ns of molecular dynamics are shown in **Figures S14** and **S15.**

We employed the following equilibration scheme:

- Initial minimization 2000 points; 1000 with steepest descent method, then conjugated gradient;
- 200 ps of NVT dynamics rising the temperature from 0 to 100 K in the first half; there is a 2.0 (kcal/mol· °A2) constraint on backbone atoms;
- 1 ns NPT dynamics rising the temperature from 100 to 150 K in the first quarter of the simulation and keeping it fixed to 150 in the rest; 1.0 (kcal/mol A2) constraint on backbone atoms;
- 1 ns NPT dynamics at 150 K with no restraints;
- 1 ns NPT dynamics rising the temperature from 150 to 200 K in the first quarter of the simulation and keeping it fixed to 200 in the rest; 1.0 (kcal/mol A2) constraint on backbone atoms;
- 1 ns NPT dynamics at 200 K with no restraints;
- 1 ns NPT dynamics rising the temperature from 200 to 250 K in the first quarter of the simulation and keeping it fixed to 250 in the rest; 1.0 (kcal/mol A2) constraint on backbone atoms;
- 1 ns NPT dynamics at 250 K with no restraints;
- 1 ns NPT dynamics rising the temperature from 250 to 300 K in the first quarter of the simulation and keeping it fixed to 150 in the rest; 1.0 (kcal/mol A2) constraint on backbone atoms;

- 1 ns NPT dynamics at 300 K with no restraints.

Production was run as 100 ns NPT dynamics, at a constant temperature of 300 K and removing all restraints, with the Langevin thermostat and Monte Carlo barostat.[2,3] A rectangular solvent box was built around each fibril model with TIP3P waters[4] with a minimum 12 Å buffer between solvent and simulation box. As all fibril models are neutral, no ion was added. Calculation of the relative energy of fibril architectures was performed extracting 100 snapshots from the 100 ns production trajectory, stripping water molecules and running a 500 step geometry relaxation on each frame using the Generalized Born implicit solvent model to attenuate steric clashes.[5,6] Results are shown in **Table S4.** Relative energy cannot be compared across different histidine protonation states (HY8d and HY8e) due to different force field parameters for ε- and δ-monoprotonated histidine.

We computed the non-covalent interaction integrals NCIIs of all fibril models to assess the strength of inter-sheet interactions. This method is based on the analysis of the promolecular electron density and provides semiquantitative information on the relative strength of non-covalent interactions.[7] According to the integration cutoffs set for the electron density, non-covalent interaction contributions can be classified as either strong attractive (**a**) or weakly attractive (**vdw**) in **Table S5.** The NCII integrals thus calculated give a measure of the strength of inter-sheet interactions only, while intra-sheet stabilizing non-covalent interactions are not taken into account. As such, they are not expected to provide a ranking of steric zipper stability, which is given by the relative energies, but rather to provide insight into the extent of residue packing at the steric zipper.

Comparing NCII values across different models, larger integral values correspond to stronger non-covalent interactions. Results, shown in **Table S4**, indicate that the strongest non-covalent interactions are established at the steric zipper of fibril model HY8e-P-FF1-UD, which is also the most favorable architecture according to the relative energies computed with Amber (**Table S4**), and can be interpreted as the most favorable side chain packing at the interface. We focused on inter-sheet interactions because as all considered fibril models are parallel, we expect intra-sheet interactions to be very similar in all cases.

Additionally, we analyzed the twist angle of the steric zipper fibril models. For each β-sheet, two vectors are defined considering strands 1 and 10 of each sheet. A vector is defined for each strand pointing from the N atom of the NHE amidated C-terminus to the carbonyl C atom of the acetylated N-terminus. The angle φ formed between the vectors of strands 1 and 10 of each β-sheet has been computed along the trajectory. The evolution of the twist angles along the MD trajectories of HY8d and H8Ye steric zipper models is presented in **Figures S16** and **S17.** Song et al.[8] have recently shown that a balance between rigidity and flexibility is key for the catalytic activity of short self-assembled peptides. Results for P-FF1-UD indicate an average twist of ~ 20 degrees for HY8e and of ~ 30 degrees for HY8d, with a more pronounced difference between the two β-sheet in HY8d than in HY8e. Both models display a certain flexibility, which would contribute to their catalytic activity in line with ref. [8] However, it has been shown in similar systems

that several twist states can be accessible by the same steric zipper architecture, and the preferred state is a complex function of environmental conditions, including sequence, growth conditions and number of protofilaments in the fibril.[9]

Supplementary figures

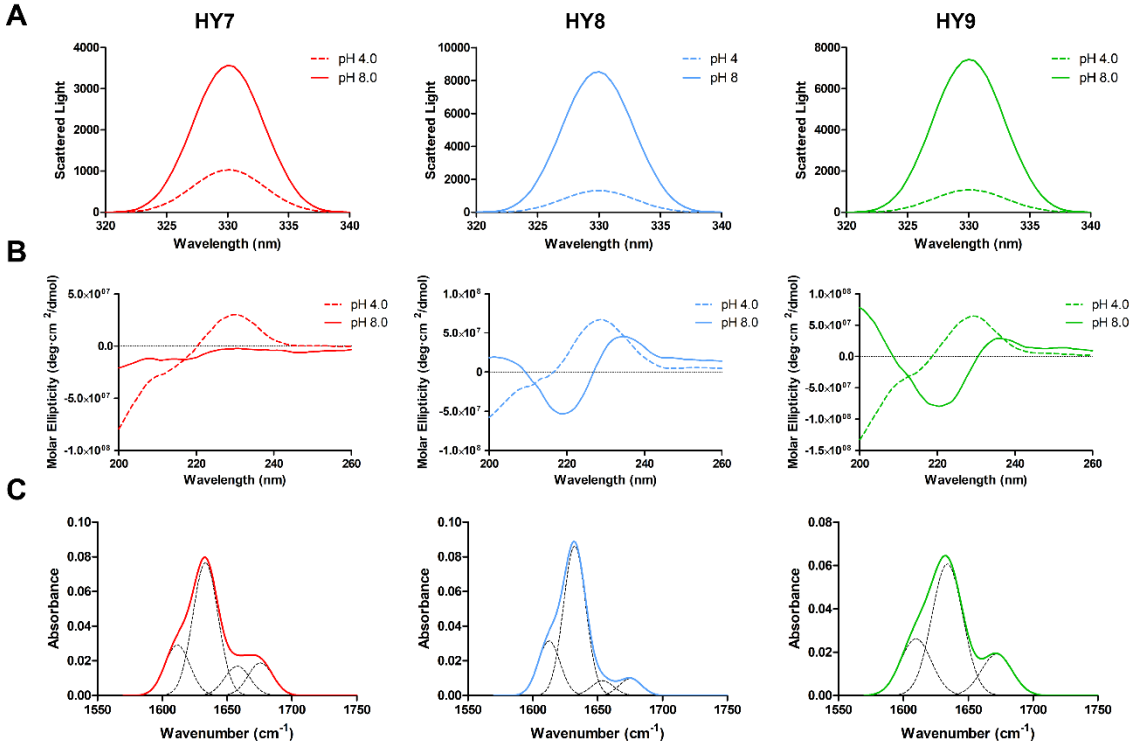

Figure S1. Conformational characterization of HY-peptides incubated at pH 4.0 and pH 8.0. HY7 (red), HY8 (blue) and HY9 (green) peptides were incubated at 250 μM at pH 8.0 (solid line) or pH 4.0 (dashed line). **A)** Synchronous light scattering. **B)** Far-UV circular dichroism spectra and **C)** FTIR absorbance spectra in the amide I region (solid line) of peptides incubated at pH 8.0. Dashed black lines indicate the different signals contributing to the spectrum.

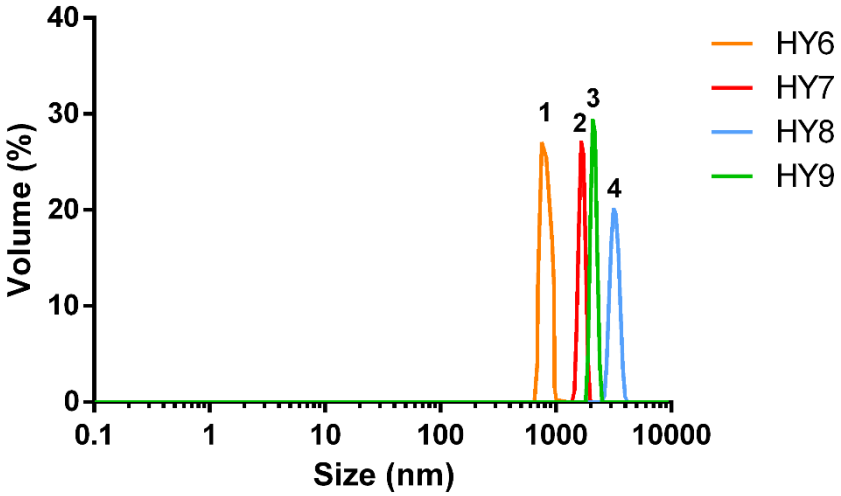

Figure S2. Size characterization of the HY6, HY7, HY8, and HY9 assemblies at pH 8.0 by DLS. Measurements displayed a single peak for each of the HY-peptides. **1** corresponds to HY6 peptide with a size of 765.7 ± 120.5 nm, **2** corresponds to HY7 peptide with a size of 1031.0 ± 453.8 nm, **3** corresponds to HY9 peptide with a size of 2097.9 ± 940.2, and **4** corresponds to HY8 peptide with a size of 3161.4 ± 1004.2 nm. Values correspond to the mean of ten measurements and the standard deviation was calculated.

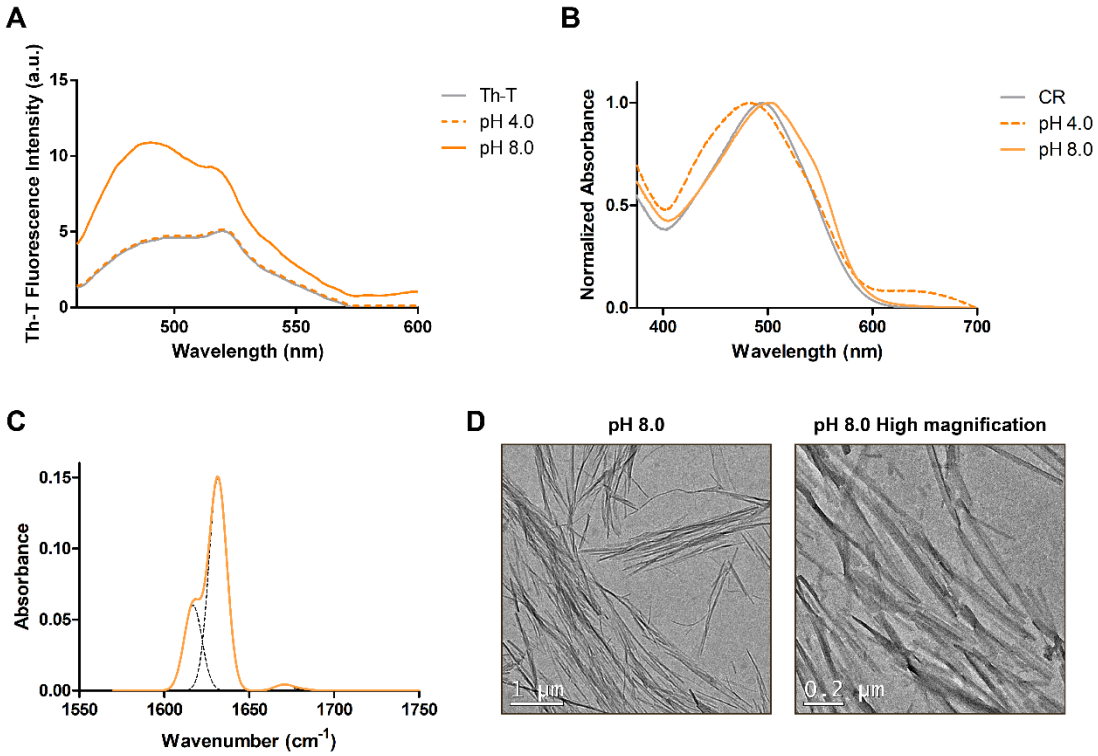

Figure S3. Characterization of the amyloid-like properties of HY6 peptide incubated at pH 4.0 and pH 8.0. The amyloid tinctorial properties of HY6 (orange) peptide were assayed using **A)** Th-T and **B)** CR. Spectra in the absence (grey line) and in the presence of HY6 peptides incubated at pH 4.0 (dashed line) and at pH 8.0 (solid line) are shown. **C)** FTIR absorbance spectrum in the amide I region of peptides incubated at pH 8. Dashed black lines indicate the different signals contributing to the spectrum. **D)** Representative micrographs of HY6 peptide samples incubated at pH 8.0. Scale bars correspond to 0.2 or 1 μm, respectively.

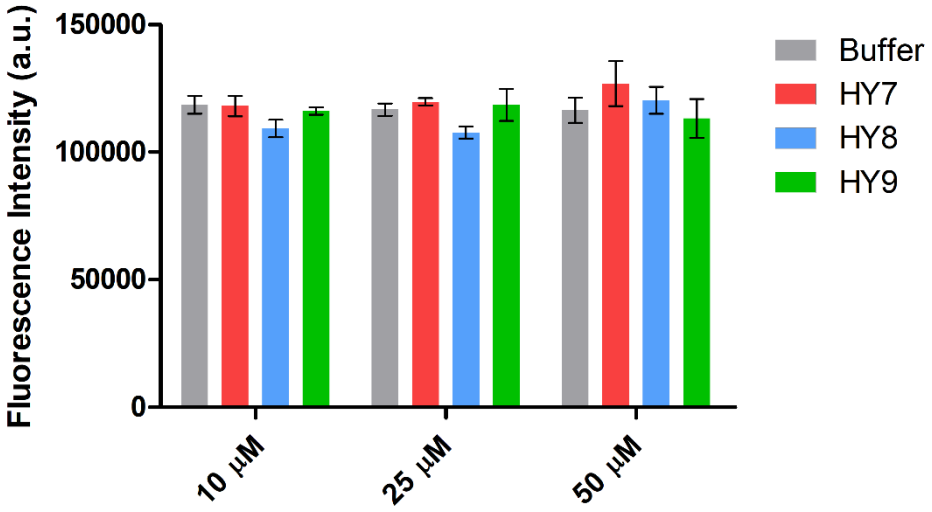

Figure S4. Cell viability assay in the presence of HY7, HY8 and HY9 peptides. Cell viability assay was performed adding 10, 25 and 50 μM of the insoluble fraction of HY7 (red), HY8 (blue) and HY9 (green) peptides incubated at pH 8.0 for 4 days at 250 μM. Data correspond to the average of two independent experiments performed in triplicates, and bars correspond to the standard deviation of the mean. Two-way ANOVA statistical test was performed comparing all samples with control. In all cases, P-value > 0.05.

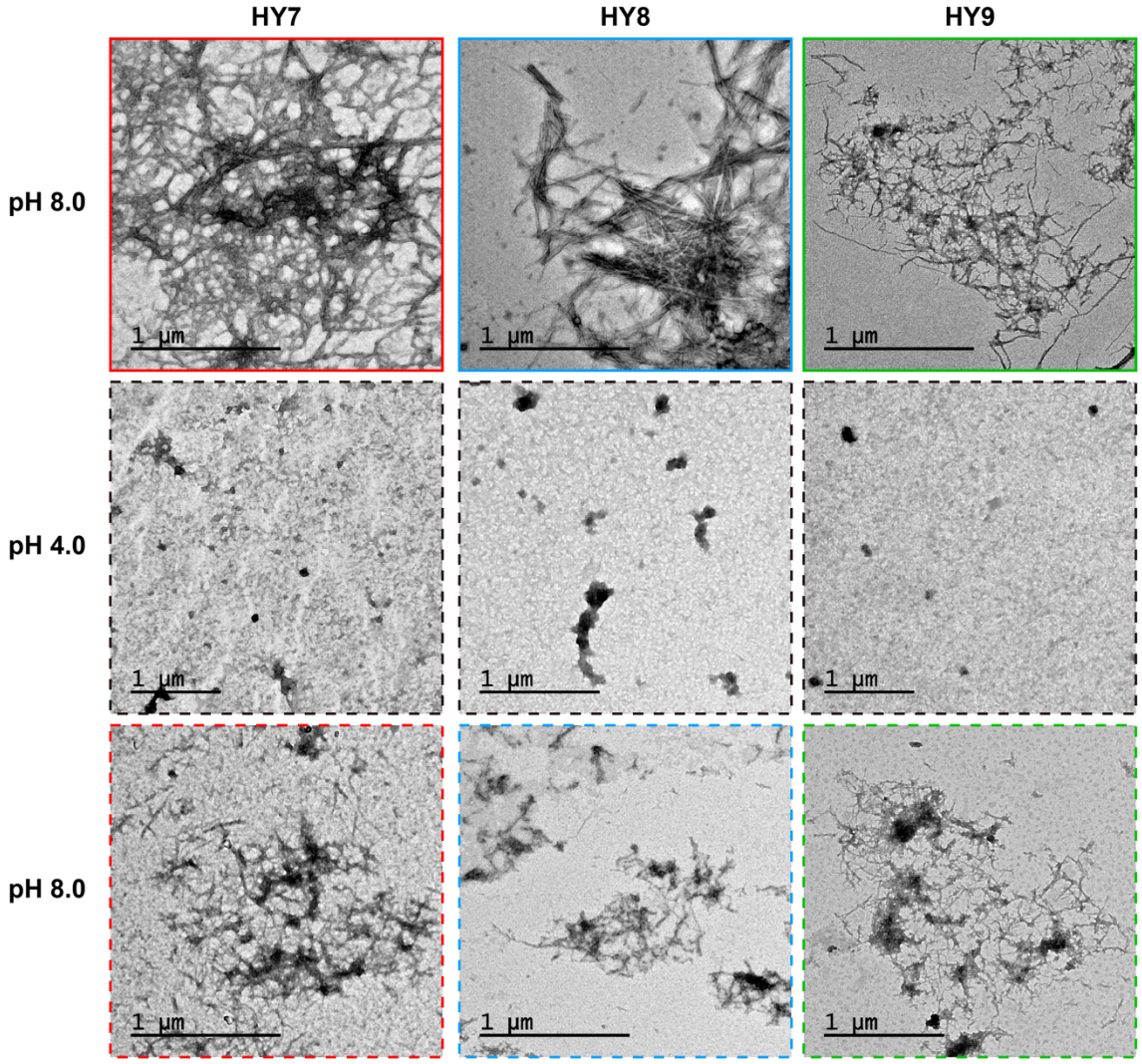

Figure S5. TEM visualization of HY7, HY8 and HY9 peptides pH-dependent assembly, disassembly and reassembly. Representative TEM micrographs obtained from incubated samples in each of the tested conditions. Continuous colored lines correspond to micrographs of pH 8.0 initial samples, dashed black lines correspond to images of their acidification to pH 4.0 and dashed colored lines correspond to reversion of the former samples back to pH 8.0. Scale bars correspond to 1 μm.

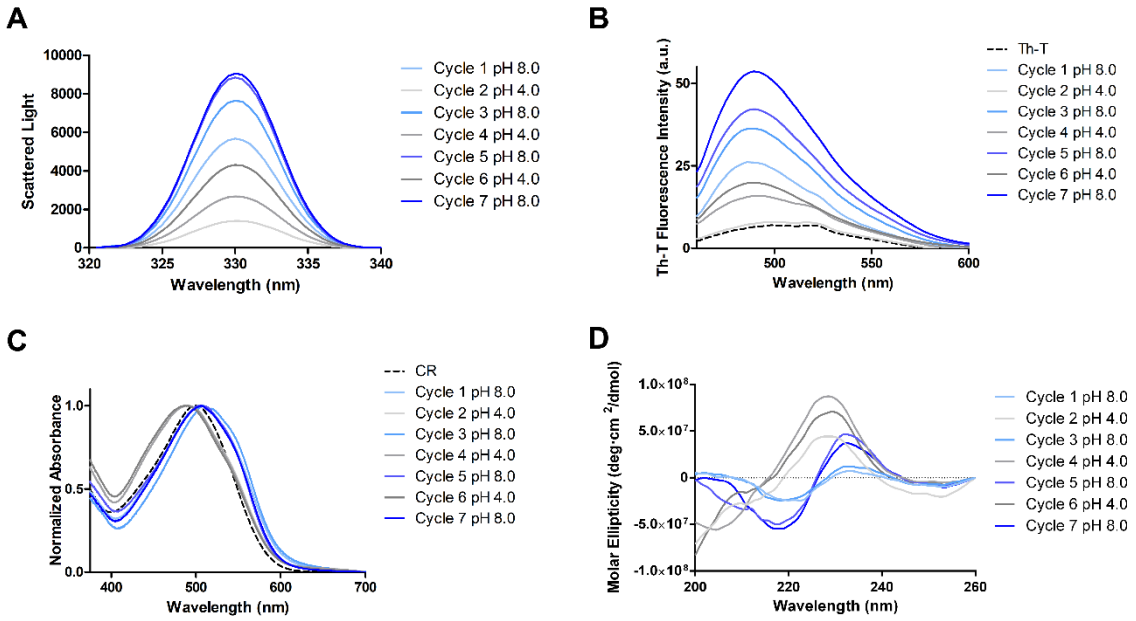

Figure S6. HY8 assembly and disassembly cycles as a function of the pH. HY8 peptide was prepared at 250 μM. A total of 4 assembling-disassembling cycles were performed corresponding cycles 1, 3, 5 and 7 to samples incubated at pH 8.0 and cycles 2, 4 and 6 to samples incubated at pH 4.0. **A)** The aggregated state of the samples was analyzed by synchronous light scattering. Amyloid tinctorial properties were assessed by **B)** Th-T and **C)** CR binding assays, performed in the absence (grey line) and in the presence (colored and black lines) of peptide. **D)** The secondary structure content of the peptides was assessed by far-UV CD.

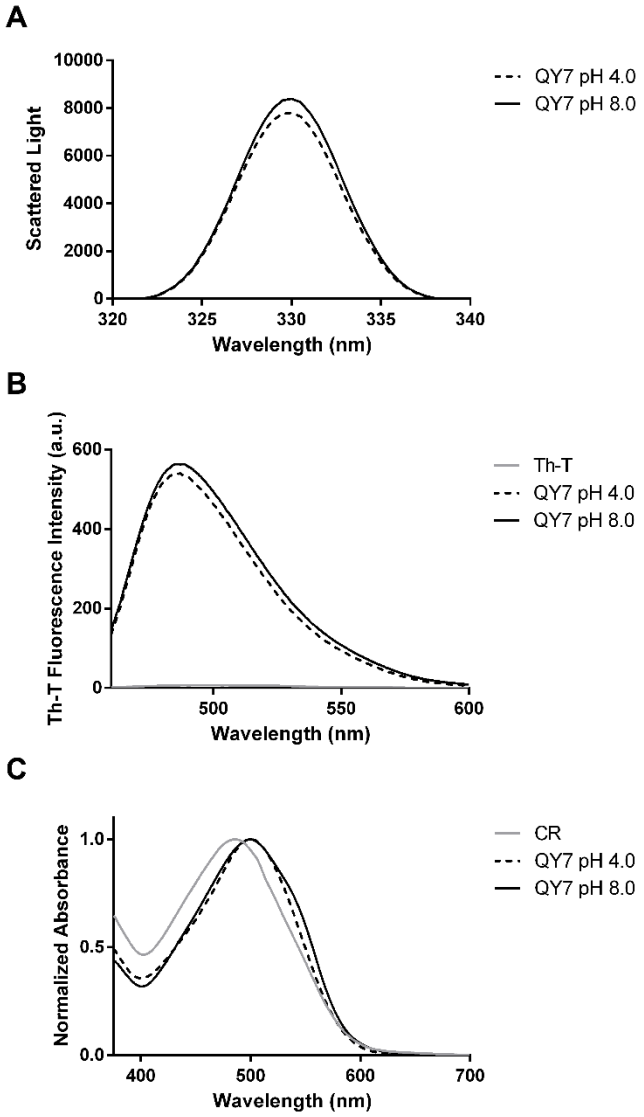

Figure S7. QY7 assembly and disassembly as a function of the pH. QY7 peptide was prepared at 250 μM at pH 8.0 and incubated for 7 days. Then, assemblies where pelleted and resuspended at pH 4.0 (dashed line) and at pH 8.0 (continuous line) and incubated for 2 days. **A)** The aggregated state of the samples was analyzed by synchronous light scattering. Amyloid tinctorial properties were assessed by **B)** Th-T and **C)** CR binding assays, performed in the absence (grey line) and in the presence (black lines) of peptide.

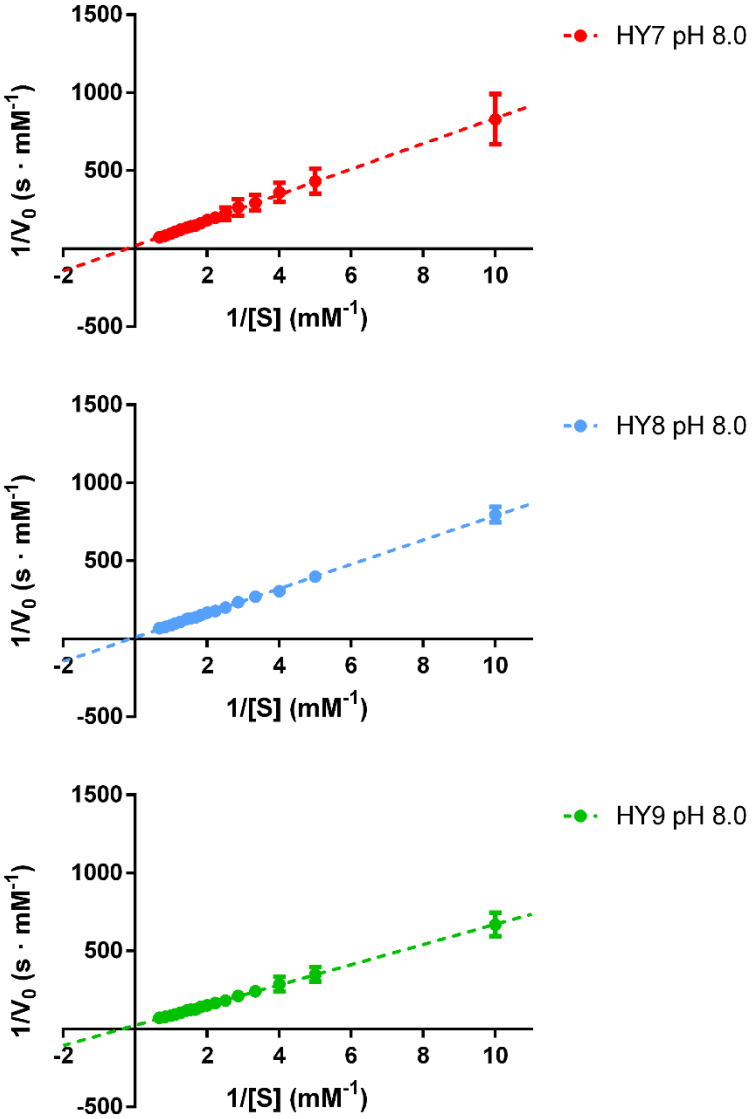

Figure S8. Lineweaver-Burk plots of pNPA hydrolysis catalyzed by 100 μM of HY7, HY8 and HY9 fibrils at pH 8.0. HY7 (red), HY8 (blue), and HY9 (green) reactions.

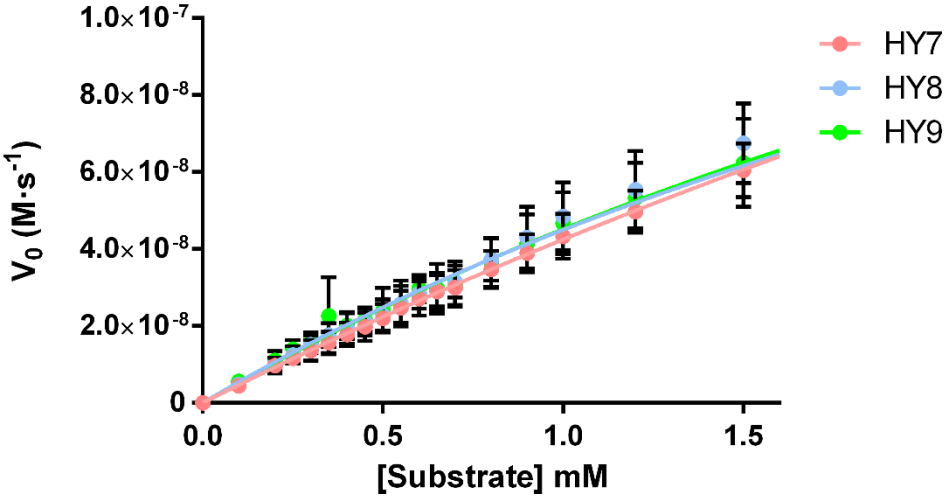

Figure S9. Catalytic activity of HY7, HY8 and HY9 fibers at pH 7.4. Esterase activity assay with HY7 (red line), HY8 (blue line), and HY9 (green line) was detected by measuring the absorbance of the yellow-colored pNP product at 405 nm in 25 mM Tris HCl pH 7.4 (E_0 concentration 100 μM). Data were fitted to the Michaelis-Menten equation with GraphPad PRISM 5.0 software.

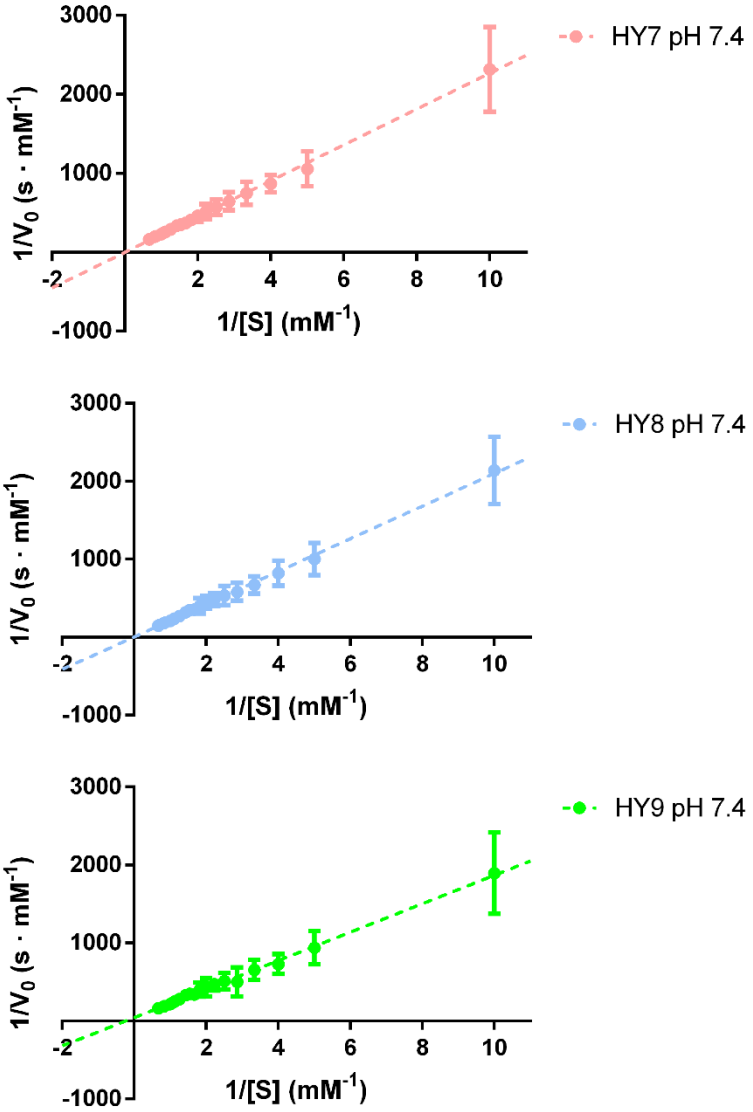

Figure S10. Lineweaver-Burk plots of pNPA hydrolysis catalyzed by 100 μM of HY7, HY8 and HY9 fibrils at pH 7.4. HY7 (red), HY8 (blue), and HY9 (green) reactions.

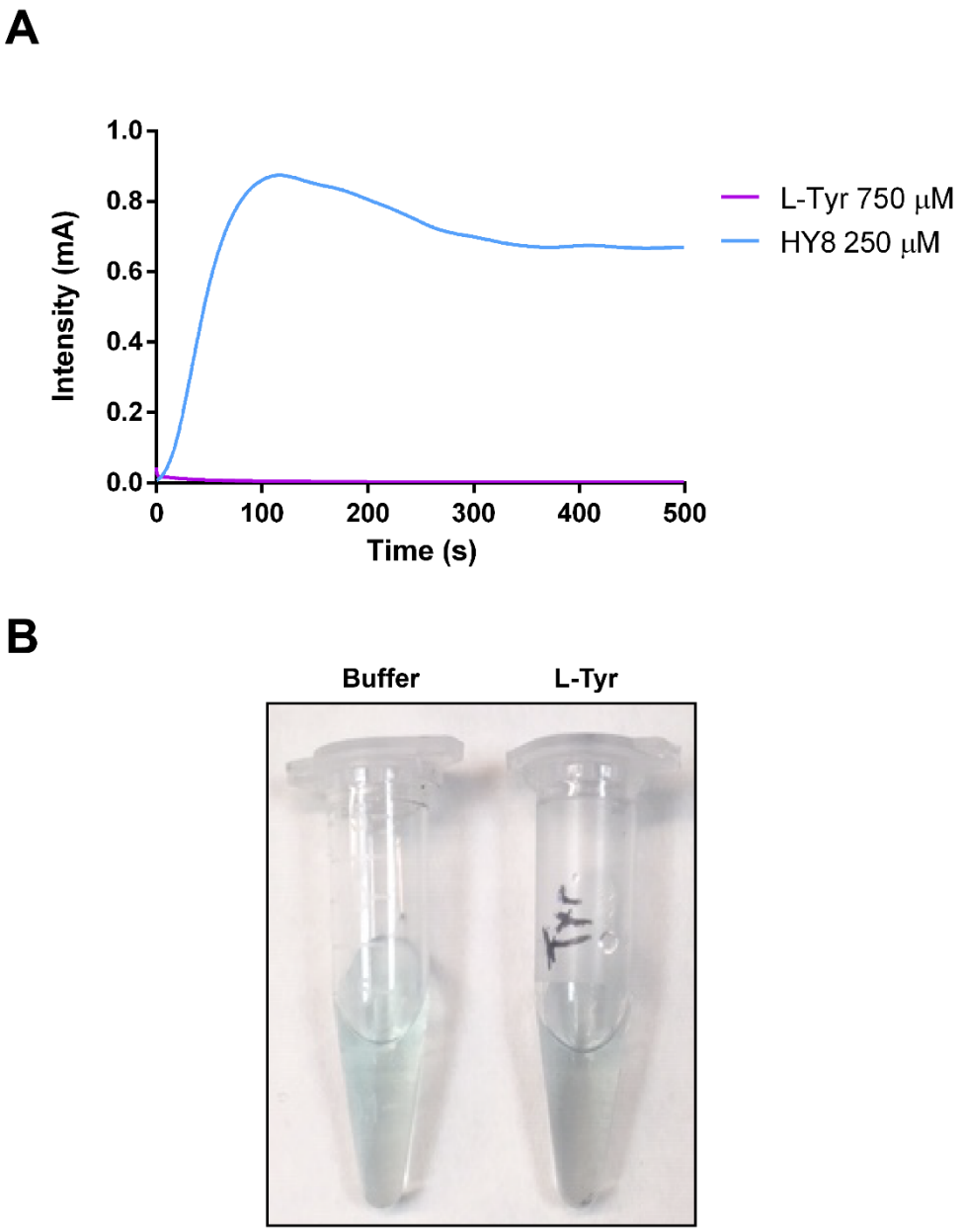

Figure S11. Electro and chemical polymerization of pyrrole by 750 μM L-Tyr at pH 8.0. **A)** Chronoamperometry (CA) curves of the electropolymerization of polypyrrole (PPy) using 750 μM of L-Tyr at pH 8.0. HY8 peptide incubated at pH 8.0 is shown as positive control of the reaction. **B)** Image of the centrifuged tubes corresponding to the chemical polymerization of buffer alone and 750 μM L-Tyr at pH 8.0 after 16 hours exposition to distilled pyrrole vapor.

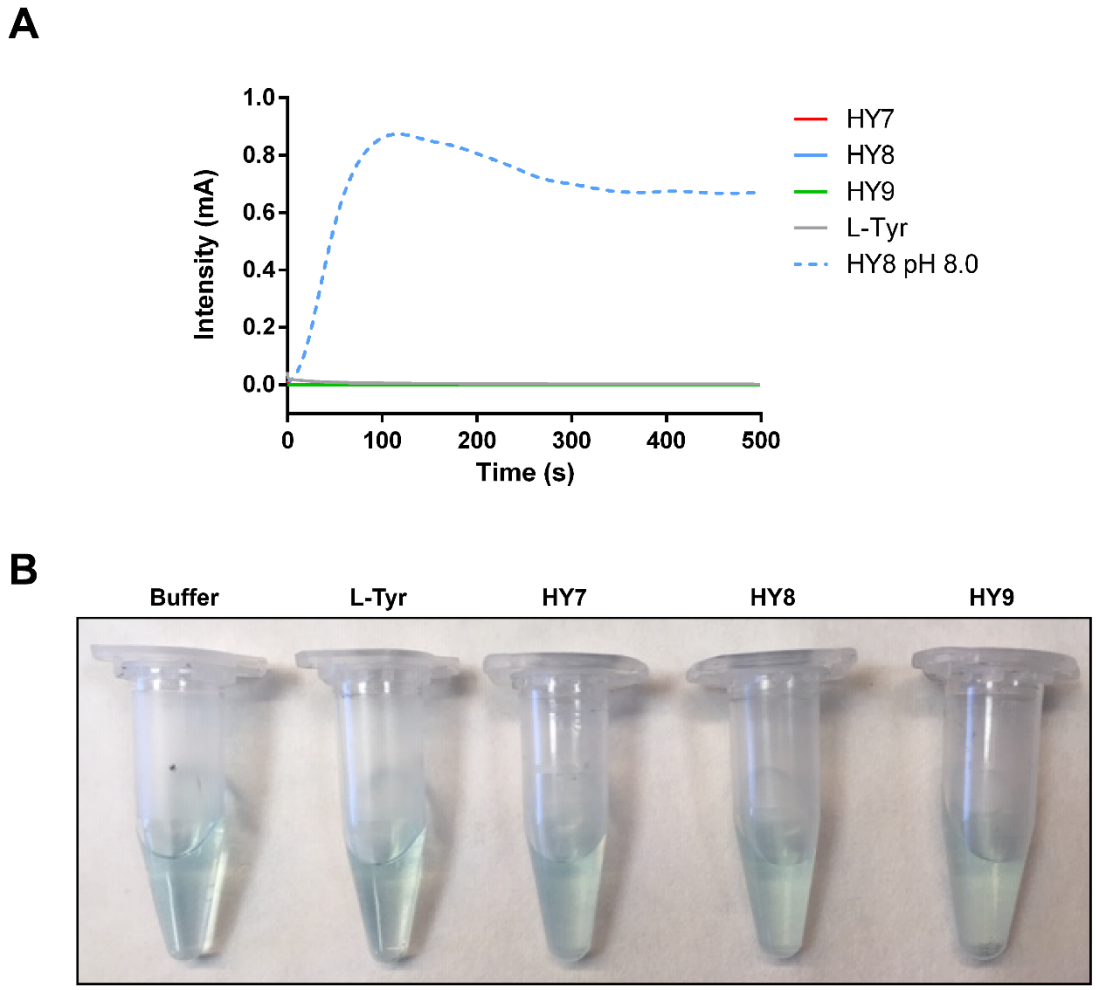

Figure S12. Electro and chemical polymerization of pyrrole by HY7, HY8 and HY9 peptides at pH 4.0. **A)** Chronoamperometry curves of the electropolymerization of polypyrrole (PPy). HY8 peptide incubated at pH 8.0 is shown as positive control of the reaction. **B)** Chemical polymerization of pyrrole by HY7, HY8 and HY9 and 750 µM L-Tyr at pH 4.0.

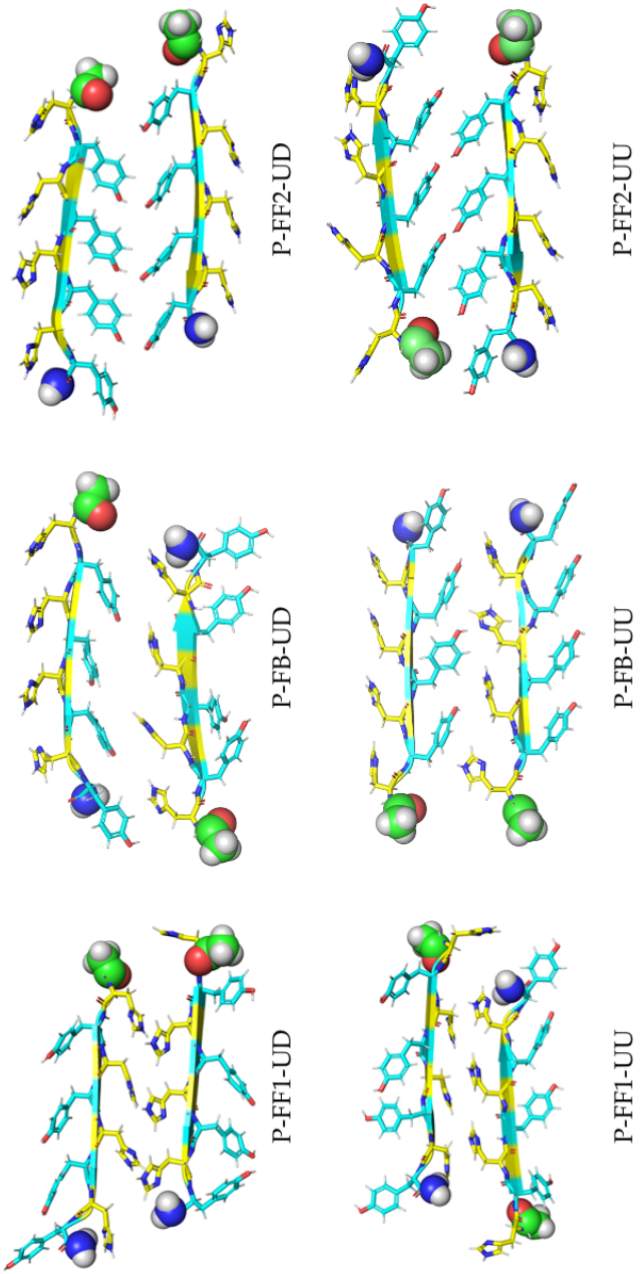

Figure S13. Residue organization at the steric zipper of the 6 analyzed parallel fibril models. Only one strand per sheet is represented. Tyrosines are represented in light blue, histidines in yellow, acetylated N-terminals in green and amidated C-terminals in blue. Fibrils nomenclature is based on the classic paper on steric zipper by Tycko;[10] P indicates that the fibril has a parallel organization, FF stands for face-to-face, FB for face-to-back, UU for up-up and UD for up-down.

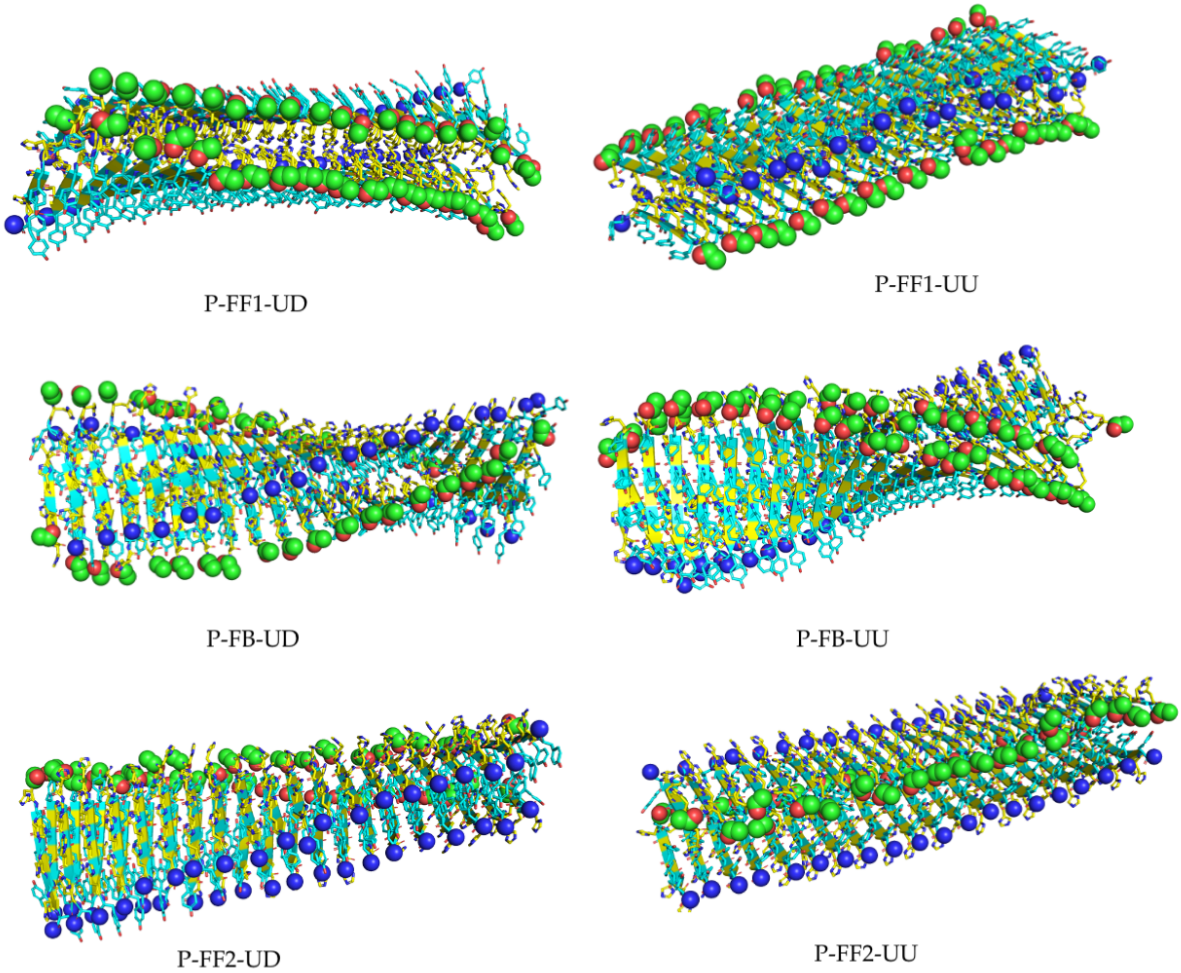

Figure S14. HY8 δ-nitrogen protonated (HY8d) fibril models after 100 ns of molecular dynamics. Tyrosines are represented in light blue, histidines in yellow, acetylated N-terminals in green and amidated C-terminals in blue. Hydrogens are omitted for clarity.

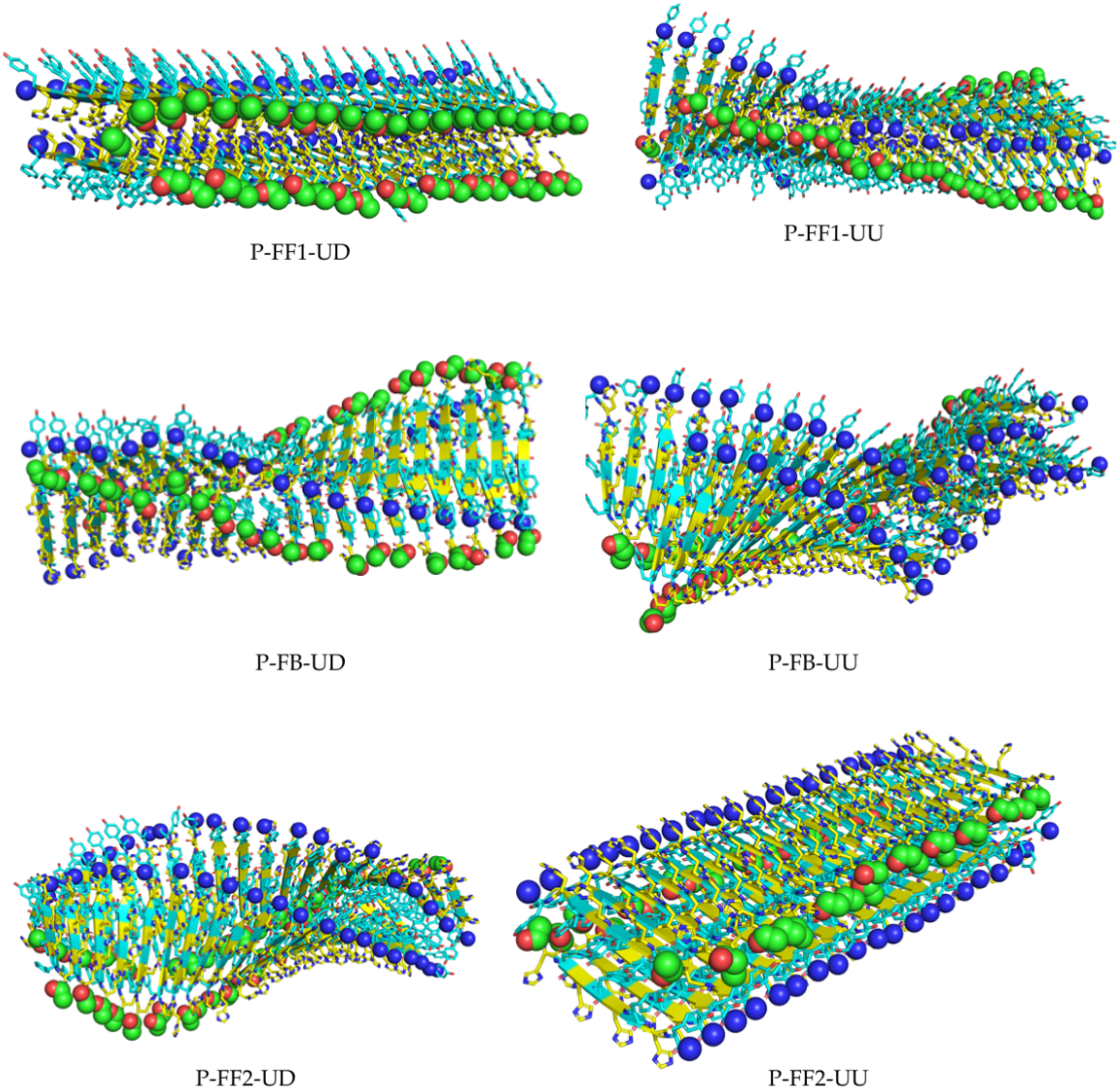

Figure S15. HY8 ε-nitrogen protonated (HY8e) fibril models after 100 ns of molecular dynamics. Tyrosines are represented in light blue, histidines in yellow, acetylated N-terminals in green and amidated C-terminals in blue. Hydrogens are omitted for clarity.

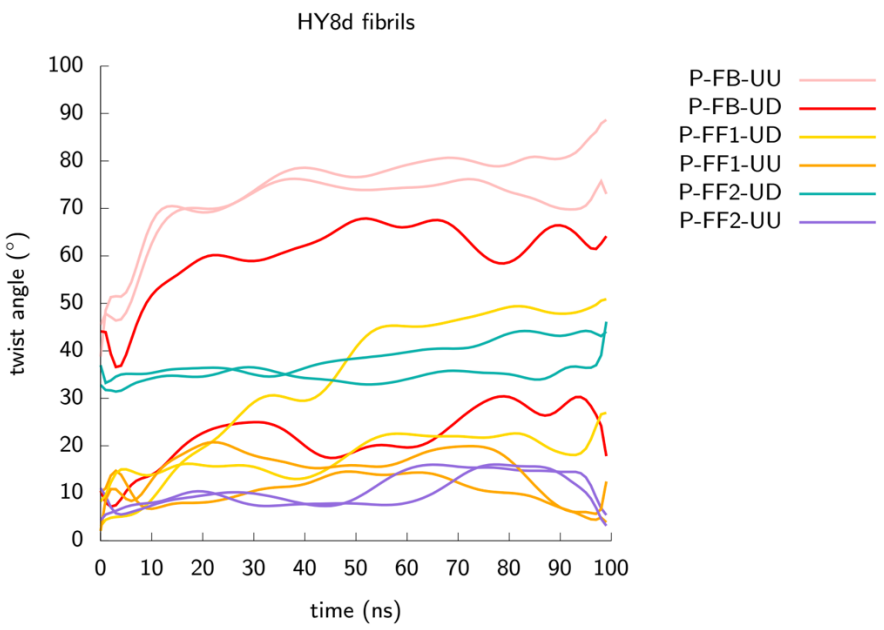

Figure S16. Evolution of the β-sheet twist angles of the six HY8d steric zipper models.

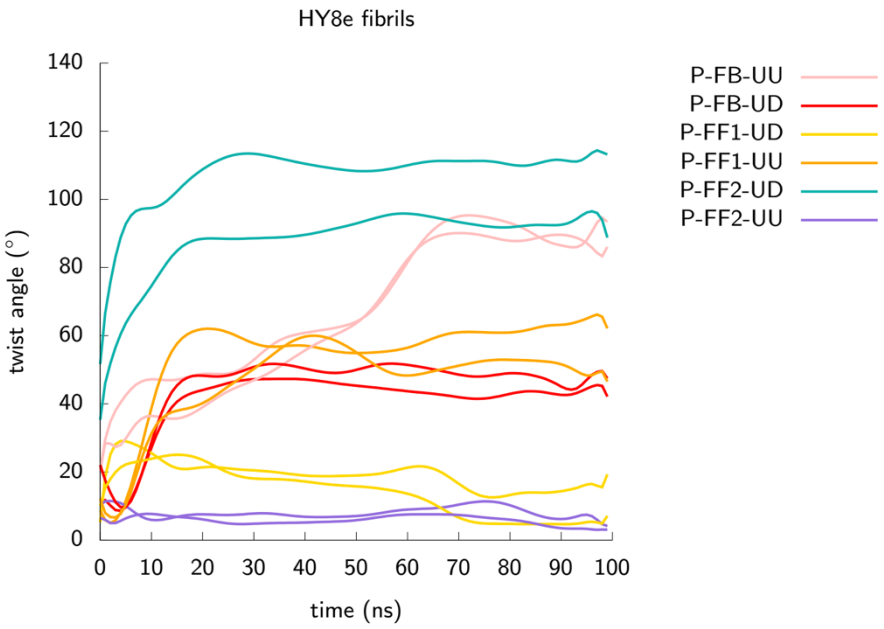

Figure S17. Evolution of the β-sheet twist angles of the six HY8e steric zipper models.

Supplementary Tables:

Table S1. FTIR secondary structure assignments. Assignment in % of the secondary structure components of HY6, HY7, HY8, and HY9 in the amide I region of FTIR spectra. The β-sheet contribution is indicated in bold.

ASSIGNMENTS		HY6	HY7	HY8	HY9
Aromatic residues	**(1610 – 1615 cm^{-1})**	28.0%	20.9%	23.1%	30.0%
Intermolecular β-sheet	**(1615 – 1636 cm^{-1})**	**69.6%**	**54.0%**	**63.4%**	**53.2%**
Disordered/Loops/Turns	**(1658 – 1662 cm^{-1})**	-	11.9%	6.3%	-
β-sheet	**(1675 – 1682 cm^{-1})**	**2.4%**	**13.2%**	**7.2%**	**16.8%**

Table S2. pH transition values from aggregation titration curves of HY7, HY8, and HY9 peptides. In the table they are shown the $pH_{1/2}$ values resulting from the fitting of the curves shown in Figure 2 to the Henderson-Hasselbalch equation, with a $R^2 > 0.95$ in all cases.

	HY7	HY8	HY9
$pH_{1/2}$	6.9	6.5	6.8
R^2	0.9627	0.9911	0.9924

Table S3. Kinetic parameters for HY7, HY8, and HY9 amyloid fibrils esterase activity at pH 8.0 and pH 7.4. Kinetic parameters were calculated from the Michaelis-Menten equation shown in Figure 5A and Figures S8, S9 and S10.

	Peptide	K_M (mM)	k_{cat} (s^{-1}) x 10^{-2}	k_{cat}/K_M (M^{-1} s^{-1})
pH 8.0	**HY7**	3.91 ± 0.96	0.49 ± 0.09	1.26 ± 0.43
	HY8	3.95 ± 0.42	0.54 ± 0.05	1.36 ± 0.18
	HY9	2.13 ± 0.33	0.35 ± 0.04	1.64 ± 0.33
pH 7.4	**HY7**	8.77 ± 3.06	0.41 ± 0.14	0.47 ± 0.49
	HY8	4.26 ± 1.07	0.23 ± 0.05	0.54 ± 0.19
	HY9	4.76 ± 1.86	0.26± 0.09	0.55 ± 0.37

Table S4. Implicit solvent Amber energies (kcal/mol) and corresponding standard deviation of the twelve HY8 fibril models. Structure labels refer to Figure S13.

	HY8d		HY8e	
	E	**stdev**	**E**	**stdev**
P-FF1-UD	-8050	20	-8782	46
P-FF2-UD	-7570	19	-8284	41
P-FB-UD	-7841	30	-8317	39
P-FF1-UU	-7943	22	-8438	28
P-FF2-UU	-7560	18	-8112	17
P-FB-UU	-7772	28	-8241	21

Table S5. Inter-sheet NCIIs of the twelve HY8 fibril models. Structure labels refer to Figure S13.

	HY8d		HY8e	
	a	**vdw**	**a**	**vdw**
P-FF1-UD	15.54	78.28	19.45	100.42
P-FF2-UD	12.48	78.25	4.33	36.44
P-FB-UD	13.25	86.68	9.50	64.33
P-FF1-UU	8.46	79.08	12.34	76.01
P-FF2-UU	13.61	90.51	13.95	89.99
P-FB-UU	10.59	44.47	8.47	54.74

References

(1) Maier, J. A.; Martinez, C.; Kasavajhala, K.; Wickstrom, L.; Hauser, K. E.; Simmerling, C. Ff14SB: Improving the Accuracy of Protein Side Chain and Backbone Parameters from Ff99SB. *J. Chem. Theory Comput.* **2015**, *11* (8), 3696–3713.

(2) Loncharich, R. J.; Brooks, B. R.; Pastor, R. W. Langevin Dynamics of Peptides: The Frictional Dependence of Isomerization Rates of N-acetylalanyl-N'-methylamide. *Biopolymers* **1992**, *32* (5), 523–535.

(3) Åqvist, J.; Wennerström, P.; Nervall, M.; Bjelic, S.; Brandsdal, B. O. Molecular Dynamics Simulations of Water and Biomolecules with a Monte Carlo Constant Pressure Algorithm. *Chem. Phys. Lett.* **2004**, *384* (4–6), 288–294.

(4) Jorgensen, W. L.; Chandrasekhar, J.; Madura, J. D.; Impey, R. W.; Klein, M. L. Comparison of Simple Potential Functions for Simulating Liquid Water. *J. Chem. Phys.* **1983**, *79* (2), 926–935.

(5) Onufriev, A.; Bashford, D.; Case, D. A. Exploring Protein Native States and Large-Scale Conformational Changes with a Modified Generalized Born Model. *Proteins Struct. Funct. Genet.* **2004**, *55* (2), 383–394.

(6) Onufriev, A.; Bashford, D.; Case, D. A. Modification of the Generalized Born Model Suitable for Macromolecules. *J. Phys. Chem. B* **2000**, *104* (15), 3712–3720.

(7) Peccati, F. NCIPLOT4 Guide for Biomolecules: An Analysis Tool for Noncovalent Interactions. *J. Chem. Inf. Model.* **2020**, *60* (1), 6–10.

(8) Song, R.; Wu, X.; Xue, B.; Yang, Y.; Huang, W.; Zeng, G.; Wang, J.; Li, W.; Cao, Y.; Wang, W.; Lu, J.; Dong, H. Principles Governing Catalytic Activity of Self-Assembled Short Peptides. *J. Am. Chem. Soc.* **2019**, *141* (1), 223–231.

(9) Periole, X.; Huber, T.; Bonito-Oliva, A.; Aberg, K. C.; Van Der Wel, P. C. A.; Sakmar, T. P.; Marrink, S. J. Energetics Underlying Twist Polymorphisms in Amyloid Fibrils. *J. Phys. Chem. B* **2018**, *122* (3), 1081–1091.

(10) Sawaya, M. R.; Sambashivan, S.; Nelson, R.; Ivanova, M. I.; Sievers, S. A.; Apostol, M. I.; Thompson, M. J.; Balbirnie, M.; Wiltzius, J. J. W.; McFarlane, H. T.; Madsen, A. Ø.; Riekel, C.; Eisenberg, D. Atomic Structures of Amyloid Cross-β Spines Reveal Varied Steric Zippers. *Nature* **2007**, *447* (7143), 453–457.